Korean Journal of Radiology

KJR

Hyperpolarized Carbon-13 Magnetic Resonance Imaging: Technical Considerations and Clinical Applications

Ying-Chieh Lai[1,2,3], Ching-Yi Hsieh[2,3,4], Yu-Hsiang Juan[1,2], Kuan-Ying Lu[1,3], Hsien-Ju Lee[3], Shu-Hang Ng[1,2], Yung-Liang Wan[1,2], Gigin Lin[1,2,3,4]

[1]Department of Medical Imaging and Intervention, Chang Gung Memorial Hospital at Linkou, Taoyuan, Taiwan
[2]Department of Medical Imaging and Radiological Sciences, Chang Gung University, Taoyuan, Taiwan
[3]Clinical Metabolomics Core Laboratory, Chang Gung Memorial Hospital at Linkou, Taoyuan, Taiwan
[4]Research Center for Radiation Medicine, Chang Gung University, Taoyuan, Taiwan

Hyperpolarized (HP) carbon-13 (^{13}C) MRI represents an innovative approach for noninvasive, real-time assessment of dynamic metabolic flux, with potential integration into routine clinical MRI. The use of [1-^{13}C]pyruvate as a probe and its conversion to [1-^{13}C]lactate constitute an extensively explored metabolic pathway. This review comprehensively outlines the establishment of HP ^{13}C-MRI, covering multidisciplinary team collaboration, hardware prerequisites, probe preparation, hyperpolarization techniques, imaging acquisition, and data analysis. This article discusses the clinical applications of HP ^{13}C-MRI across various anatomical domains, including the brain, heart, skeletal muscle, breast, liver, kidney, pancreas, and prostate. Each section highlights the specific applications and findings pertinent to these regions, emphasizing the potential versatility of HP ^{13}C-MRI in diverse clinical contexts. This review serves as a comprehensive update, bridging technical aspects with clinical applications and offering insights into the ongoing advancements in HP ^{13}C-MRI.

Keywords: Hyperpolarized; Carbon 13; Magnetic resonance imaging; Pyruvate; Lactate

INTRODUCTION

In routine clinical MRI, the proton (^{1}H) nucleus serves as the signal source due to its nearly 100% natural abundance and substantial gyromagnetic ratio, rendering it exceptionally responsive to magnetic fields. However, carbon (C), another important nucleus of the human body, has also garnered substantial research interest. Although carbon-12 (^{12}C) has an abundance of 98.9%, its ground-state nuclear spin is zero, rendering it inactive for MRI applications (Supplementary Fig. 1). In contrast, carbon-13 (^{13}C) possesses a ground-state nuclear spin of 1/2,

rendering it MRI-active. Nevertheless, ^{13}C possesses only a quarter of the gyromagnetic ratio of ^{1}H and a lower natural abundance of 1.1%. Consequently, to expand the utilization of ^{13}C MRI in clinical scenarios, an essential process known as hyperpolarization is necessary to significantly enhance the signal of ^{13}C.

Dynamic nuclear polarization (DNP) is a hyperpolarization technique that has been successfully implemented in clinical human studies. It enhances the polarization of solid-state ^{13}C labeled compounds by subjecting them to extremely low temperatures and high magnetic fields, followed by rapid liquid dissolution (Supplementary Fig. 2) [1]. Hyperpolarized carbon-13 (HP ^{13}C)-MRI has emerged as a promising method for metabolic imaging with clinical potential, significantly boosting the signal-to-noise ratio by up to 50000-fold. This enhancement facilitates the detection of probe signals and downstream metabolites in clinical MRI scanners, illustrating their potential impact in clinical settings. The primary probe frequently used in HP ^{13}C-MRI is [1-^{13}C]pyruvate, in which the ^{13}C label is positioned at the C1 site of the pyruvate molecule. Once transported to cells via the monocarboxylate transporter 1 (MCT1), this compound is converted by lactate

dehydrogenase (LDH) into [1-^{13}C]lactate. This metabolic pathway is a valuable indicator of the Warburg effect [2]. Concurrently, [1-^{13}C]pyruvate can follow alternative metabolic routes, such as its conversion into [1-^{13}C]alanine within the cytosol via alanine aminotransferase (ALT), or into ^{13}C-bicarbonate within the mitochondria through pyruvate dehydrogenase (PDH). Notably, the C1 position of [1-^{13}C]pyruvate remains uninvolved in the tricarboxylic acid (TCA) cycle. Consequently, monitoring the TCA flux can only be achieved indirectly by evaluating the pyruvate-to-bicarbonate flux. In contrast, [2-^{13}C]pyruvate, specifically labeled at the C2 position, directly enters the TCA cycle, facilitating the direct observation of TCA intermediates, as illustrated in Figure 1.

HP ^{13}C-MRI provides unique benefits compared to other molecular imaging techniques, such as positron emission tomography (PET) [3]. Unlike PET, which depends on radioactive tracers, HP ^{13}C-MRI employs non-radioactive compounds, thereby enhancing its safety and suitability for repeated imaging studies. Moreover, HP ^{13}C-MRI provides sufficient spatial and temporal resolution, enabling the real-time visualization of metabolic flux in living organs.

The acquisition of HP ^{13}C-MRI takes only a few minutes and can be seamlessly integrated into routine clinical MRI scans. In contrast, the most commonly used radiotracer in PET/CT, 2-deoxy-2-[^{18}F]fluoroglucose (FDG), captures only cellular glucose uptake and the initial glycolysis step [4]. This limitation prevents the monitoring of downstream metabolism. HP ^{13}C-MRI, on the other hand, features high spectral resolution, allowing for discrimination of the metabolic fates of [1-^{13}C]pyruvate. This capability enables the monitoring of metabolic pathways beyond the initial step of glycolysis, thereby providing a more comprehensive understanding of metabolism. A comparison between HP

Table 1. Comparison between HP ^{13}C-MRI and PET

	HP ^{13}C-MRI	PET
Radiation	No	Yes
Procedure time, mins	2–3	30
Multiple tracer	Yes	No
Downstream metabolism	Yes	No
Cost	Very high	High
Clinical applications	Under research	Well established

HP = hyperpolarized
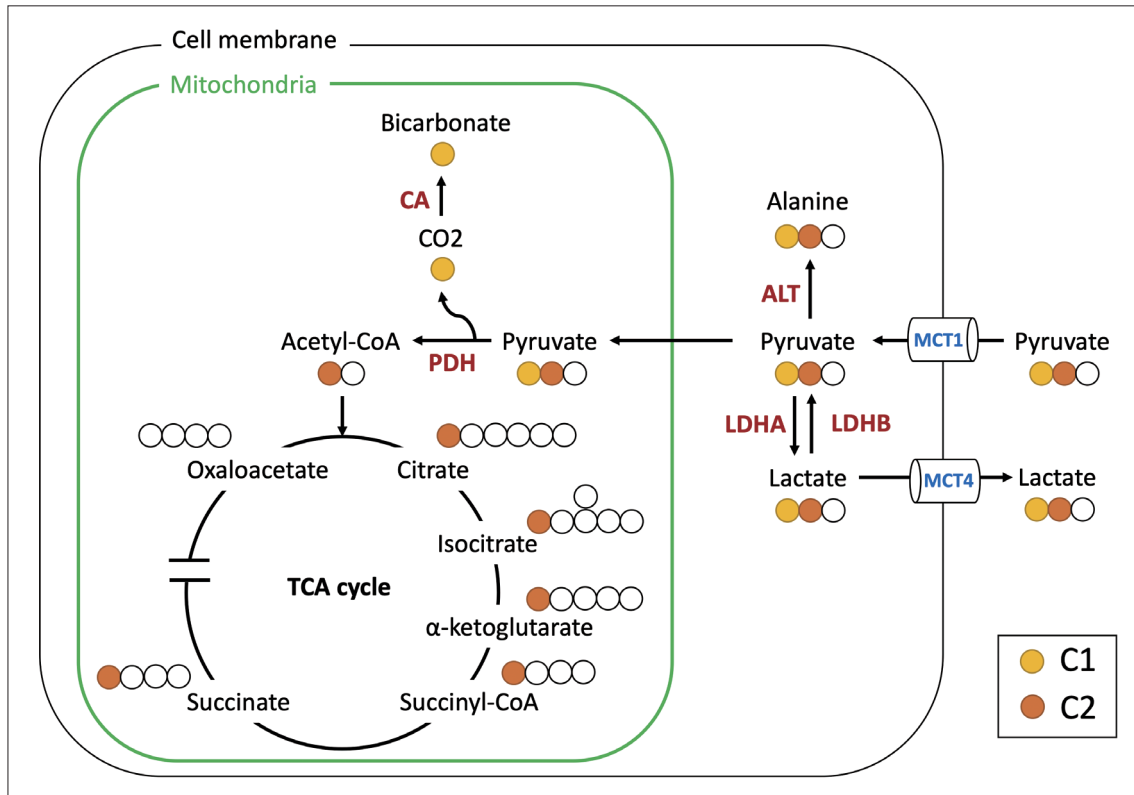
Fig. 1. Principal metabolic pathways of [1-^{13}C]pyruvate and [2-^{13}C]pyruvate that were detected by hyperpolarized ^{13}C-MRI. For comparison of the metabolic fates of pyruvate's C1 and C2, the C1 and C2 ^{13}C positions are indicated in yellow and orange, respectively. CA = carbonic anhydrase, PDH = pyruvate dehydrogenase, ALT = alanine transaminase, MCT = monocarboxylate transporter, LDH = lactate dehydrogenase

^{13}C-MRI and FDG-PET is shown in Table 1.

To effectively implement HP ^{13}C-MRI in clinical settings, specific hardware, pharmaceutical techniques, robust data acquisition approaches, and standardized analyses are essential. This article provides an in-depth review of the technical aspects and potential clinical uses of HP ^{13}C-MRI.

Technical Considerations for Clinical HP ^{13}C-MRI

Multidisciplinary Team for HP ^{13}C-MRI

Initiating a clinical team for HP ^{13}C-MRI necessitates the assembly of a proficient group of MRI physicists, pharmacists, and radiologists. Acquiring a research license for tracers is of paramount importance, particularly when focusing on the development of investigative medicinal products. Similar to the procedures followed for developing new PET tracers, the process of submitting an Investigational New Drug (IND) application for a novel ^{13}C-labeled probe involves providing the FDA with comprehensive documentation, including chemistry, manufacturing, and control procedures; preclinical safety pharmacology and toxicology data; dosimetry data; and a clinical protocol. These submissions lay the groundwork for initiating human trials [5]. For probes that have already received IND approval, for example, [1-^{13}C]pyruvate in the U.S., obtaining authorization for distribution in other countries still necessitates approval from the respective nation's drug regulatory authorities. This ensures that safety and quality control standards are maintained during probe production at local manufacturing sites. In addition, to foster collaborative efforts, teams should establish a healthcare institution referral pathway and create a seamless network for research and development partnerships. While initial endeavors may revolve around research pursuits, the primary objective is to secure regulatory approval for diagnostic use, underscoring a commitment to compliance and upholding the highest standards of patient care throughout the process.

Clinical Workflow of HP ^{13}C-MRI

A clinical human HP ^{13}C-MRI study requires specialized equipment, including a clinical polarizer to polarize ^{13}C-labeled probes and a multinuclear MRI scanner equipped with specialized radiofrequency (RF) transmit-receive coils tailored for ^{13}C acquisition [6]. The polarizer is typically positioned near the MRI scanner to reduce the probe transportation time. The clinical workflow of HP ^{13}C-MRI

is well established and involves 1) probe preparation, 2) hyperpolarization (DNP), 3) dissolution and quality control, 4) imaging acquisition, and 5) data analysis. The clinical workflow of HP ^{13}C-MRI is summarized in Figure 2.

Probe Preparation

This process involves mixing good manufacturing practice-grade ^{13}C-labeled probes with electron paramagnetic agents (EPAs) and a minimal quantity of gadolinium-binding contrast agent [7]. The mixture is then loaded onto a commercially available sterile fluid path designed for polarizer use. The preparation must adhere to sterile techniques and be conducted in a sterile clean room.

Hyperpolarization

Except for the initial investigation, the vast majority of clinical applications of HP ^{13}C-MRI in human subjects utilize the SPINlab polarizer (GE Healthcare, Chicago, IL, USA) [6]. In a clinical polarizer, functioning at 0.8 K and 5T, the mixture exists in a solid state. Owing to the EPAs' higher susceptibility to the magnetic field, an initial polarization build-up occurs within the EPAs. Subsequently, the polarization of the EPAs' unpaired electrons is transferred to nearby ^{13}C nuclei via microwave irradiation at a specific frequency [8]. This DNP process, taking approximately 2–3 hours, results in a 20%–40% polarization level, leading to a signal amplification exceeding four orders of magnitude [1].

Dissolution and Quality Control

After the dissolution is initiated, pressurized and superheated sterile water is used to rapidly dissolve the solid-state probe. The resulting solution is passed through a filter to remove the EPAs and neutralized with a buffer solution. Finally, the solution is passed through a sterile filter to remove potential pathogens. Before administration to the patient, the final solution undergoes rigorous quality control checks, including evaluation of temperature (25°C–37°C), pH (5–9), EPA concentrations ($\leq$ 5 µM), pyruvate concentrations (200–280 mM), and polarization levels ($\geq$ 10%). In addition, the integrity of the sterile filter is verified using a bubble point test, ensuring that it exceeds 50 pounds per square inch (PSI) [9]. These measures ensure that the imaging probe is safe, effective, and of the highest quality for clinical applications. Notably, the utilization of deuterium oxide (D_2O) as a solvent for [1-^{13}C]pyruvate has recently been demonstrated to be a safe and practical approach for maintaining polarization and enhancing the signal-to-noise ratio [10].
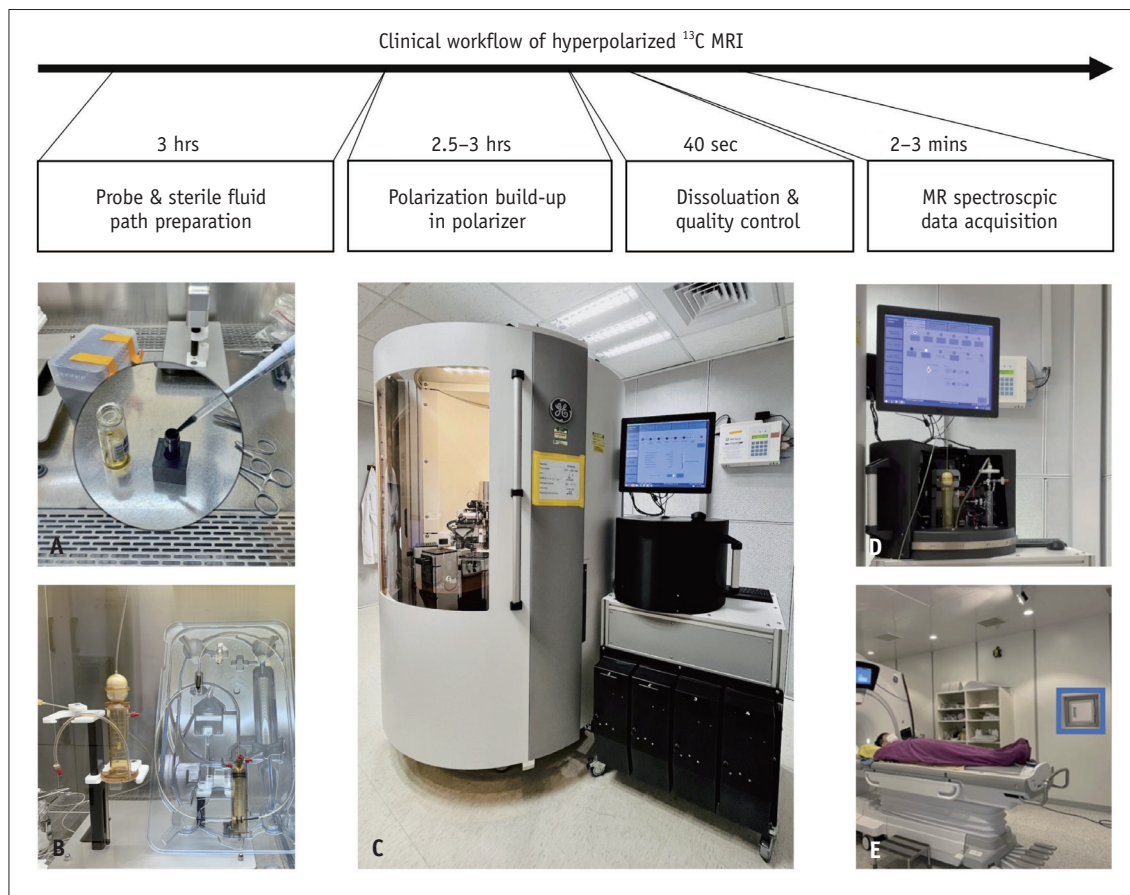
Fig. 2. Clinical workflow of hyperpolarized ^{13}C-MRI. **A:** In a controlled, clean room equipped with a laminar flow hood, the drug was prepared by blending a ^{13}C-labeled probe with EPAs and gadolinium. **B:** The pre-mixed drug was introduced into a sterile fluid path assembly, which included a dissolution syringe (containing sterile water for injection), a sample vial (housing the probe), an EPA filter, a receiver vessel (containing buffer solution), and an administration syringe for injection. **C:** A clinical polarizer, designed for human research, operates within a high magnetic field and an ultra-low-temperature environment. The buildup of polarization typically takes 2–3 hours to reach a polarization level of 20%–40%. **D:** Following the initiation of dissolution, superheated and pressurized water dissolved the solid-state sample, and the resulting solution underwent filtration and buffering processes. The solution, comprising the hyperpolarized probe, underwent meticulous quality control measures. **E:** The hyperpolarized probe was subsequently transported to an MRI scanner for administration in human subjects. The ^{13}C signal was promptly and efficiently acquired using optimized pulse sequences. EPA = electron paramagnetic agent

Imaging Acquisition

Prior to gathering data, it is essential to calibrate the ^{13}C central frequency, fine-tune the transmit gain, and optimize the magnetic field through shimming [11,12]. After dissolution, the hyperpolarized state becomes transient and returns to its thermal equilibrium state after leaving the polarizer. This transition creates a limited time window of 2–3 min for signal acquisition, depending on the spin-lattice relaxation time (T1). To maximize this brief window, flip angles usually range from 10° to 30° to manage the nonrecoverable hyperpolarized magnetization. Using small flip angles helps preserve the magnetization for longer experiments, albeit at the cost of signal strength and resolution [13].

The following MRI sequences are commonly used in HP ^{13}C-MRI. Fast spectroscopic imaging methods, such as echo planar spectroscopic imaging (EPSI), achieve a speed advantage with multi-echo readouts; however, they face compromises in spectral bandwidth, spatial resolution, and signal-to-noise ratio efficiency [14-17]. In contrast, model-based imaging, such as Iterative Decomposition of water and fat with Echo Asymmetry and Least-square estimation (IDEAL) chemical shift imaging, accelerates spectral encoding and reduces scan times when metabolite chemical shifts and the B_0 field map are known. However, this method carries the risk of noise amplification and is vulnerable to motion and frequency shifts [18]. Another option, metabolite-specific imaging, is an extremely fast technique

Table 2. Comparison of pulse sequences in hyperpolarized ^{13}C-MRI

Sequence	Advantages	Challenges
Fast spectroscopic imaging	Faster by employing multi-echo readouts; still providing continuous spectral coverage; robust for frequency shifts	Limited spectral bandwidth, spatial resolution, and SNR efficiency; relatively slow because of the requirement for phase encoding; susceptible to motion
Model-based imaging	More efficient phase encoding because only relative metabolite chemical shift required	Requires prior knowledge of both metabolite chemical shifts and B_0 field map; lower temporal resolution compared to metabolite-specific imaging; susceptible to both motion and frequency shifts
Metabolite-specific imaging	Fastest acquisition method for single metabolite; robust to motion	Requires spectra with sparce and well separated peaks; easy for variable flip angle schemes; susceptible to frequency shifts

SNR = signal-to-noise ratio

that uses spectral-spatial (SPSP) RF pulses to excite a single metabolite, followed by a rapid imaging readout, such as echoplanar or spiral [19,20]. The acquisition then shifts the center frequency to the next metabolite and cycles through the resonances of each metabolite of interest. The use of variable flip-angle schemes can be used to enhance the signal-to-noise ratio of the metabolic products because each metabolite is excited separately [21]. The advantages and challenges of these sequences are summarized in Table 2.

Data Analysis

In the quantification of dynamic ^{13}C spectral data acquired through HP ^{13}C-MRI, two prevalent methodologies are often employed: kinetic modeling and model-free metrics (Fig. 3). Kinetic modeling entails the development of a mathematical model that delineates the rates at which ^{13}C-labeled probes undergo conversion into products, accounting for factors such as relaxation and RF pulse effects. For example, for [1-^{13}C]pyruvate, the pyruvate-to-lactate conversion rate constant, commonly denoted as k_{PL}, is frequently used to characterize glycolytic activity [22]. Beyond the two-site exchange model, more intricate models have been devised to accommodate additional factors, such as vascular perfusion and cellular uptake, rendering them more physiologically realistic. However, because of the increased number of parameters, these models can become more susceptible to instability during model fitting [23].

Model-free metrics have gained traction as viable alternatives to kinetic models. Among these metrics, metabolite ratios have emerged as the predominant choice, in which the substrate or total ^{13}C signal is used as the denominator. In the context of dynamic ^{13}C spectra, the area under the curve (AUC) is a fundamental tool for calculating ratios [24]. These ratios provide a straightforward approach for assessing metabolic conversion and possess inherent normalization, rendering them highly resilient to fluctuations in polarization levels, RF coil sensitivities, and perfusion. However, it is important to note that these AUC ratios may require correction in instances where variable flip angles are employed during the acquisition process.

Clinical Applications

The first human HP ^{13}C-MRI using [1-^{13}C]pyruvate was a significant milestone in medical imaging and cancer research. This study, conducted in 2013, involved patients with prostate cancer and demonstrated the feasibility and safety of this technique. Subsequently, this approach has been applied to various organs and diseases. Table 3 summarizes the clinical applications of HP ^{13}C-MRI, and Supplementary Table 1 contains the in-depth quantitative results from human studies [25-56].

Brain

Tailored imaging and treatment strategies are essential for brain tumors because of their diverse behaviors, emphasizing the need for ongoing research and innovative approaches, such as HP ^{13}C-MRI. Miloushev et al. [25] conducted the first study on the human brain, discovering non-uniform lactate production from pyruvate, with increased levels observed in the cortical and subcortical regions. Additionally, they noted variability in glycolytic activity across various gliomas and brain metastases. Meanwhile, Autry et al. [26] conducted a pivotal study of HP ^{13}C-MRI in brain tumors involving five patients with glioma and three healthy volunteers. Their findings affirmed HP ^{13}C-MRI's reliability in providing data on pyruvate conversion to lactate and bicarbonate within the brain tissues. Notably,
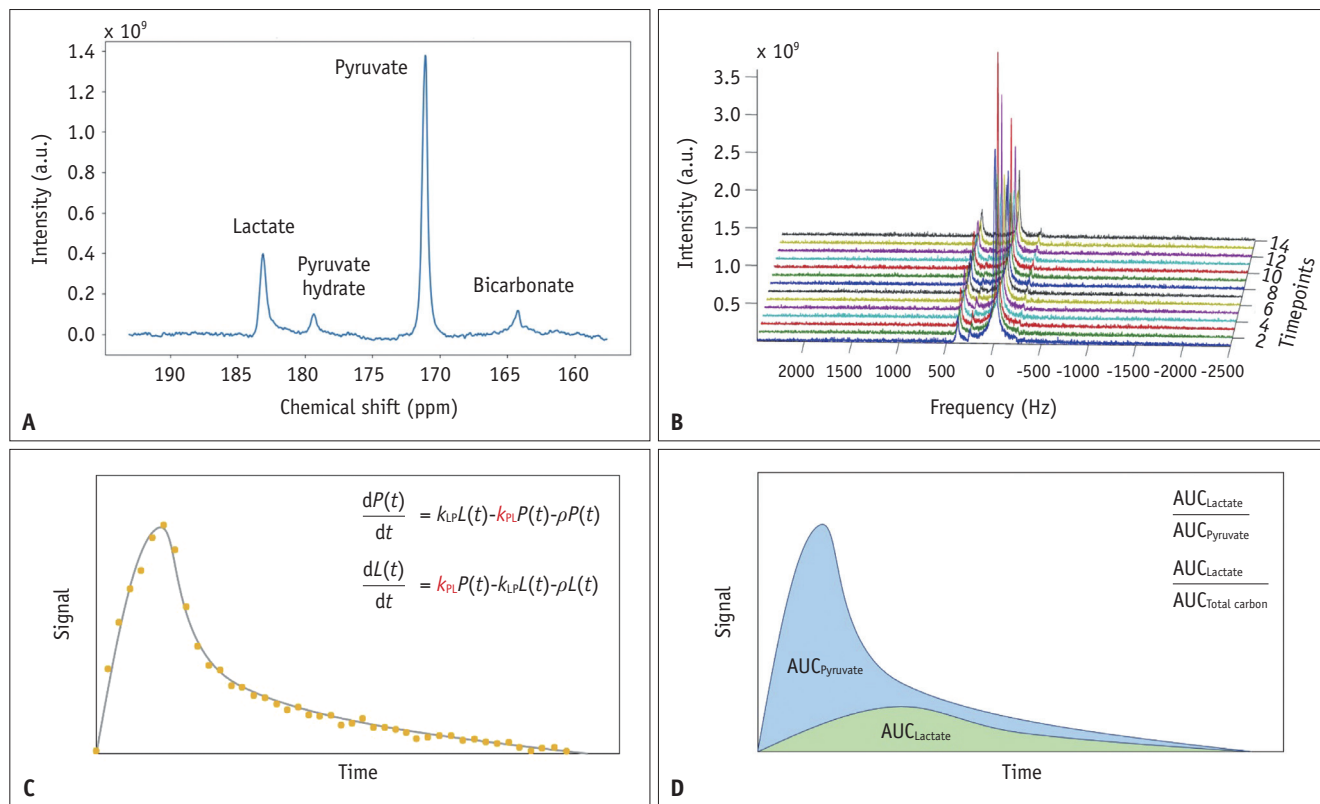
Fig. 3. Representative data and key quantitative methods for pyruvate-to-lactate conversion in hyperpolarized ^{13}C-MRI. **A:** A representative single timepoint ^{13}C spectrum was dominated by the resonance from [1-^{13}C]pyruvate (171 ppm), [1-^{13}C]lactate (183 ppm), [1-^{13}C]pyruvate hydrate (179 ppm), and [^{13}C]bicarbonate (164 ppm). **B:** Stacked plot of dynamic ^{13}C spectra with a temporal resolution of 2 s. **C:** Kinetic modeling involves creating a mathematical model to describe the conversion rates of ^{13}C-labeled probes into various products. The conversion rate constant, often denoted as k_{PL}, serves as a key parameter for characterizing the speed of the pyruvate-to-lactate flux. **D:** Metabolite ratios, often in the form of AUC ratios, employ the AUC of the product as the numerator and either the substrate or the total ^{13}C signal as the denominator, offering an alternative approach to evaluate the pyruvate-to-lactate flux. AUC = area under the curve

treatment with bevacizumab, an anti-vascular endothelial growth factor (VEGF) antibody, increased pyruvate conversion rates, which was attributed to its impact on the blood-brain barrier.

Gliomas with isocitrate dehydrogenase (IDH) mutations have a favorable prognosis. In IDH-mutant glioblastomas, higher pyruvate-to-lactate conversion rates were observed, with the contrast-enhancing region showing a higher conversion rate than the T2 hyperintense region [26,30]. Conversely, IDH wild-type glioblastomas show lower pyruvate-to-lactate conversion [29]. Nevertheless, multiple studies have consistently reported reduced bicarbonate production in brain tumors compared to normal brain tissue [26,29,30]. These studies indicate that HP ^{13}C-MRI has the potential to evaluate intertumoral heterogeneity in tumor metabolism. Furthermore, the application of ^{13}C-MRI extends beyond glioblastomas to pediatric brain tumors, including diffuse intrinsic pontine gliomas, demonstrating the safe and

efficient use of this novel technique in pediatric patients [27]. Additionally, Lee et al. [28] studied intracranial brain metastases and used pre-treatment HP ^{13}C-MRI lactate signals to predict tumor progression after stereotactic radiosurgery, achieving a positive predictive value of 0.8 (Fig. 4A).

The blood–brain barrier's permeability to pyruvate has been confirmed by the detection of both lactate and bicarbonate signals in the human brain following intravenous [1-^{13}C]pyruvate injection, with metabolite signals being more prominent in the cortex than in the white matter [31,32,34]. An investigation demonstrated consistently elevated lactate and bicarbonate signals in specific cerebral regions, such as the precuneus, cuneus, and lingual gyrus, which were segmented according to the Human Brain Atlas. This highlights HP ^{13}C-MRI's capability to assess spatial metabolic variations in the human brain, suggesting its potential as an alternative to traditional functional brain

Table 3. Summary of clinical applications from the human studies using hyperpolarized ^{13}C-MRI

| Authors	N	Targets	Clinical applications
Brain			
Miloushev et al., 2018 [25]	4	Glioma and metastasis	1st human brain tumor study
Autry et al., 2020 [26]	8	Infiltrative glioma	Post radio-chemotherapy follow-up
Autry et al., 2021 [27]	10	Pediatric brain tumor	Tumor vs. normal brain, safety profile
Lee et al., 2021 [28]	11	Intracranial metastasis	Prediction of radiotherapy response
Chen et al., 2021 [29]	3	Glioblastoma	Tumor vs. normal brain
Zaccagna et al., 2022 [30]	8	Glioblastoma	Tumor vs. normal brain
Grist et al., 2019 [31]	4	Normal brain	Technical feasibility in human brain
Lee et al., 2020 [32]	14	Normal brain	Metabolite topography in human brain
Hackett et al., 2020 [33]	2	Brain trauma	Traumatic brain injury
Ma et al., 2022 [34]	4	Normal brain	Technical feasibility in human brain
Uthayakumar et al., 2023 [35]	35	Brain aging	Metabolic changes in brain aging
Heart and skeletal muscle			
Cunningham et al., 2016 [36]	4	Heart	1st human healthy heart study
Rider et al., 2020 [37]	10	Heart	Healthy heart vs. diabetic heart
Park et al., 2020 [38]	9	Heart	Cardiotoxicity of doxorubicin
Ma et al., 2022 [39]	3	Heart	End diastolic vs. end systolic
Park et al., 2021 [40]	9	Calf skeletal muscle	Rest vs. exercise vs. recovery
Body and oncology			
Woitek et al., 2020 [41]	1	Breast cancer	Post neoadjuvant chemotherapy follow-up
Woitek et al., 2021 [42]	7	Breast cancer	Very early neoadjuvant chemotherapy response
Tran et al., 2019 [43]	1	Renal cell carcinoma	Intratumoral metabolic heterogeneity
Tang et al., 2021 [44]	11	Renal cell carcinoma	Tumor grade and histopathologic type
Ursprung et al., 2022 [45]	9	Renal cell carcinoma	Prediction of tumor grade
Lee et al., 2022 [46]	13	Liver, kidney, pancreas, spleen	Normal intrabdominal solid organs
Stødkilde-Jørgensen et al., 2020 [47]	2	Pancreatic cancer	Tumor vs. normal
Gordon et al., 2023 [48]	6	Pancreatic cancer	Tumor vs. normal, early response prediction
Nelson et al., 2013 [49]	31	Prostate cancer	1st human study, safety profile, tumor vs. normal
Aggarwal et al., 2017 [50]	1	Prostate cancer	Early response for androgen deprivation therapy
Chen et al., 2020 [51]	6	Prostate cancer, metastatic castration-resistant	Feasibility in bone and liver metastasis
Granlund et al., 2020 [52]	12	Prostate cancer	Tumor grade of prostate cancer
de Kouchkovsky et al., 2021 [53]	1	Prostate cancer, metastatic castration-resistant	Early immunotherapy response assessment
Chen et al., 2022 [54]	5	Prostate cancer	Integration with MR/TRUS fusion-guided biopsy
Sushentsev et al., 2022 [55]	10	Prostate cancer, intermediate risk	Metabolic phenotyping in intermediate risk prostate cancer
Lin et al., 2024 [56]	6	Cervical cancer	Immune activation of spleen

N = number, TRUS = transrectal ultrasound

MRI [32]. In patients with mild traumatic brain injury, focal changes at the injured site revealed decreased bicarbonate levels and increased lactate production without apparent anatomical alterations [33]. Uthayakumar et al. [35] employed HP ^{13}C-MRI to measure the whole-brain metabolism in individuals of various ages. Their findings showed a 7% decrease in lactate and a 9% decrease in bicarbonate levels per decade, with distinct spatial variations in the rates of change among different brain regions.

Heart and Skeletal Muscle

Cunningham et al. [36] performed the first human heart HP ^{13}C-MRI utilizing the electrocardiogram (EKG)-gated fast metabolic imaging technique (SPSP) in healthy volunteers. They observed the downstream metabolism of pyruvate with lactate in both chambers and the myocardium, and
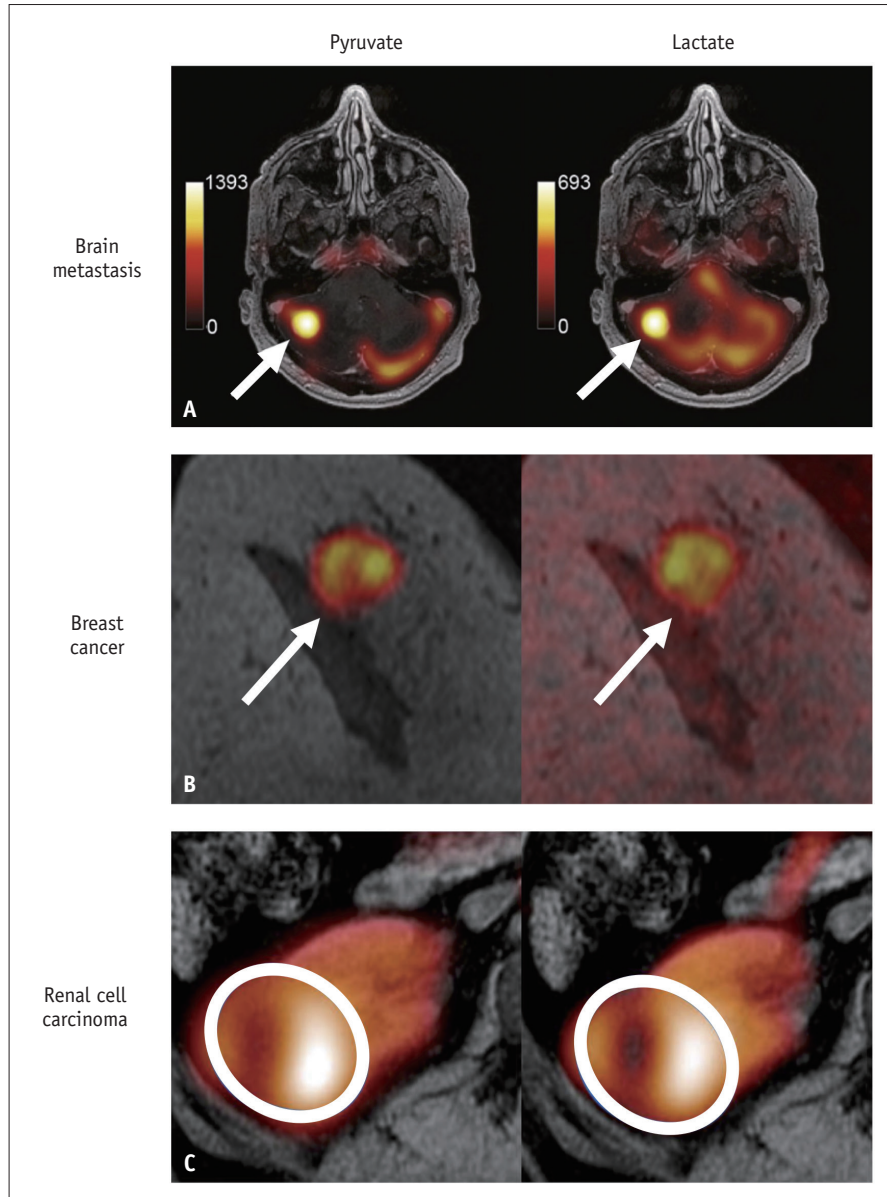
Fig. 4. Examples of clinical applications of hyperpolarized ^{13}C-MRI, where pyruvate and lactate maps are overlayed with anatomic [1]H-MRI. **A:** Right cerebellar metastasis from renal cell carcinoma (arrows) (Adapted from Lee et al. *J Neurooncol* 2021;152:551-557 [28], with permission of CC BY 4.0 license). **B:** Right breast cancer (arrows) (Adapted from Woitek et al. *Radiol Imaging Cancer* 2020;2:e200017 [41], with permission of Radiological Society of North America). **C:** Renal cell carcinoma in the right kidney (Adapted from Ursprung et al. *Cancers (Basel)* 2022;14:335 [45], with permission of CC BY 4.0 license).

bicarbonate only in the myocardium. This finding highlights the significance of bicarbonate in the assessment of cardiac metabolism. Meanwhile, in a study comparing heart metabolism in healthy volunteers and patients with type 2 diabetes mellitus (DM), a significant reduction in pyruvate-to-bicarbonate flux was observed in the hearts of patients with type 2 DM, and an oral glucose challenge before HP ^{13}C-MRI was found to enhance bicarbonate production [37]. Similarly, EKG gating's importance in imaging heart

metabolism was emphasized in a dual-phase acquisition study at the end systolic and diastolic phases, with the bicarbonate-to-lactate ratio being significantly smaller at end diastolic phase, influenced by coronary flow and cyclical metabolic changes [39]. Transitioning to monitoring tumor metabolism, HP ^{13}C-MRI can assess cancer treatment-related adverse events, as observed in a study by Park et al. [38] investigating doxorubicin-induced cardiotoxicity in breast cancer patients. They observed a decrease in the bicarbonate
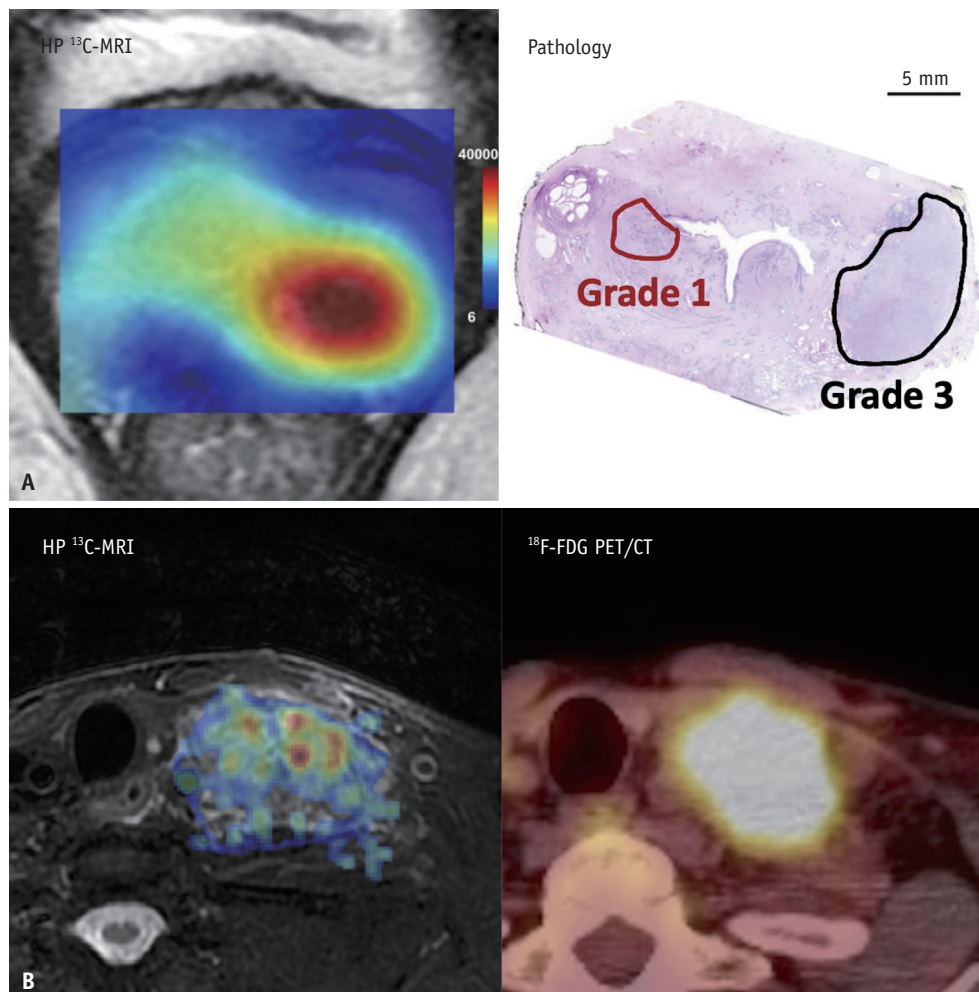
Fig. 5. Aligning HP ^{13}C-MRI with established diagnostic procedures. **A:** The lactate signal-to-noise ratio map in the HP ^{13}C-MRI (left panel) correlates to the histopathology analysis (right panel) and distinctly showcases a stronger lactate signal in the grade 3 prostate cancer located in the left peripheral zone, as opposed to the weaker signal observed in the grade 1 prostate cancer in the right transition zone, which illustrates of the correlation of the Warburg effect and the tumor grade (Adapted from Sushentsev et al. *Nat Commun* 2022;13:466 [55], with permission of CC BY 4.0 license). **B:** Comparative analysis of HP ^{13}C-MRI and ^{18}F-FDG PET/CT in assessing the left neck metastatic lymph node (level IV) from a patient with head and neck cancer. It shows a [1-^{13}C]pyruvate map superimposed on a fat-suppressed T2-weighted image (right panel), alongside an ^{18}F-FDG map overlaid on a CT scan (left panel). HP = hyperpolarized, FDG = 2-deoxy-2-[^{18}F]fluoroglucose

signal after doxorubicin treatment, indicating its potential to improve patient care. Furthermore, in another study by Park et al. [40], the impact of exercise on pyruvate metabolism in human skeletal muscles was investigated. They found that in the imaged calf muscles, bicarbonate production increased 8.4-fold after exercise and returned to baseline after resting, whereas lactate continued to rise, increasing by 3.3-fold compared to baseline, even after resting.

Breast

Gallagher et al. [57] demonstrated HP ^{13}C-MRI's potential in breast cancer grading by analyzing lactate-to-pyruvate ratios

(Lac/Pyr), with all grade 3 tumors showing lactate signals, but not grade 2 tumors. In subsequent studies aimed at the early prediction of treatment response, Lac/Pyr was found to increase 7–11 days after neoadjuvant chemotherapy, and a 20% threshold increase in Lac/Pyr effectively differentiated responders from non-responders (Fig. 4B) [41,42]. These studies underline HP ^{13}C-MRI's potential to enhance treatment response prediction in breast cancer.

Liver, Kidney, and Pancreas

Conducting HP ^{13}C-MRI in the liver presents a challenge because of the dual perfusion system of the portal vein and

hepatic artery. Peak perfusion of the liver occurs during the portovenous phase, typically 70–90 s after administration of the contrast medium. Unfortunately, this time limit is suboptimal for achieving the most advantageous acquisition window for the HP ^{13}C signals. In addition, on HP ^{13}C-MRI of the abdomen, it was evident that the liver exhibited a lower metabolite signal than the kidney, pancreas, and spleen. Nevertheless, the liver is a highly metabolic organ, displaying the highest rates of pyruvate-to-lactate and pyruvate-to-alanine conversion among intra-abdominal solid organs [46]. The use of HP ^{13}C-MRI to study liver parenchymal diseases, including hepatic steatosis, fibrosis, and malignancies, is presently undergoing thorough investigation [58].

Studies have suggested that HP ^{13}C-MRI can provide valuable metabolic information for diagnosing and grading renal tumors. Tran et al. [43] demonstrated intratumoral metabolic heterogeneity in human renal cell carcinoma (RCC). Similarly, Tang et al. [44] used HP ^{13}C-MRI to assess the lactate-to-pyruvate ratio in various RCC subtypes, with chromophobe RCC having the highest ratio, followed by grade 3 clear-cell RCC and grade 2 clear-cell RCC. Additionally, Ursprung et al. [45] confirmed the correlation between increased k_{PL} values and higher tumor grade in RCC (Fig. 4C) and noted that renal liposarcomas and pheochromocytomas had metabolic activity similar to that of grade 4 RCC, while benign oncocytomas had lower k_{PL} values.

Despite the technical challenge of the decreased signal-to-noise ratio of the pancreas due to its central location in the abdomen, Stødkilde-Jørgensen et al. [47] successfully acquired metabolic signals from pancreatic cancers in two patients. The alanine signal primarily originated from the tumor and the lactate signal was distributed in both cancerous and normal pancreases. Subsequently, Gordon et al. [48] demonstrated comparable findings, revealing lower alanine-to-lactate ratios in cancerous pancreatic tissues than in healthy pancreatic tissues. Additionally, initial metabolic responses observed four weeks after post-chemotherapy were found to correlate with later changes in tumor size.

Prostate

Prostate cancer, the second most prevalent cancer among men worldwide, presents diagnostic and treatment complexities primarily owing to its varying clinical manifestations, ranging from indolent to highly aggressive tumors with the potential to metastasize. Nelson et al. [49] performed the first-in-human study of 31 patients with prostate cancer using [1-^{13}C]pyruvate and demonstrated the safety and potential of characterizing tumor metabolism. They observed increased pyruvate-to-lactate conversion in cancerous areas, encouraging further HP ^{13}C-MRI clinical trials. Subsequently, Chen et al. [51] extended the use of HP ^{13}C-MRI to assess bone and liver metastases in prostate cancer. They found a higher pyruvate-to-lactate conversion in metastatic tumors than in primary tumors, indicating a higher tumor grade. Additionally, chemotherapy led to a reduction in pyruvate-to-lactate conversion in treated liver metastases.

Early response assessment is crucial in cancer care and in guiding treatment adjustments to enhance patient outcomes and survival. Aggarwal et al. [50] showed a substantial reduction in pyruvate-to-lactate flux in prostate cancer after anti-androgen therapy despite limited tumor size changes on T2-weighted images and modest changes in apparent diffusion coefficient images. HP ^{13}C-MRI offers promise for early metabolic assessment and prediction of treatment responses. Assessing the treatment response in bone metastases using traditional imaging is challenging because of bone sclerosis and unreliable size measurements. A previous study demonstrated k_{PL} reduction in bone metastases after 8 weeks of immune checkpoint inhibitor therapy, preceding observable size changes [53]. This study also highlighted the value of HP ^{13}C-MRI for early response assessment.

Prostate cancer varies from low-risk indolent tumors to aggressive malignancies, and intratumoral heterogeneity challenges the accuracy of biopsies. HP ^{13}C-MRI exhibits promise in assessing this complexity. Granlund et al. [52] showed that lactate levels increase with the Gleason tumor grade in prostate cancer, a process driven by MCT1 and associated with PTEN loss. Similarly, Sushentsev et al. [55] studied patients with intermediate-risk prostate cancer (Gleason 7; PSA < 20 ng/mL). They found a positive correlation between lactate signal-to-noise ratio and Gleason pattern 4, suggesting HP ^{13}C-MRI's value in distinguishing significant from indolent prostate cancers (Fig. 5A). Transitioning to alternative approaches, magnetic resonance imaging (MRI)-guided transrectal ultrasound (TRUS) biopsy combines MRI and TRUS guidance to obtain prostate tissue samples for cancer detection and treatment planning. Nevertheless, HP ^{13}C-MRI is an emerging technique for the detection of hidden prostate cancer. Notably, Chen et al. [54] integrated HP ^{13}C-MRI and conventional MRI to guide TRUS biopsy, achieving success in five patients using a k_{PL}

value above 0.02 as a cancer marker. As a result, half of the analyzed ^{13}C-positive biopsy cores were found to be cancerous. This approach enhances the detection accuracy of MRI-guided TRUS biopsies.

Future Directions of HP ^{13}C-MRI

Beyond pyruvate, a diverse array of innovative agents has either received clinical approval or are currently considered to have clinical potential, as summarized in Table 4 [59-68]. For instance, the metabolic activity of the TCA cycle in healthy human brains was investigated by analyzing the conversion of [2-^{13}C]pyruvate to [5-^{13}C]glutamate [61]. Additionally, [^{13}C,[15]N$_2$]urea administered without subsequent metabolism has been identified as a valuable tool for assessing tissue perfusion dynamics [62,63]. The IDH mutation, a critical biomarker in glioblastoma, is specifically interrogated using [1-^{13}C]α-ketoglutarate, which transforms into [1-^{13}C]2-hydroxyglutarate [64]. Moreover, intratumoral pH is a crucial indicator of tumor aggressiveness, and [1-^{13}C]1,2-glycerol carbonate serves as a non-invasive pH imaging probe [65,66]. Furthermore, [2-^{13}C]dihydroxyacetone was designed to evaluate hepatic glycolysis, gluconeogenesis, and glycerol synthesis [67], whereas [1,4-[13]C$_2$]fumarate has been used to probe necrosis [68].

Introducing copolarization as an innovative technique allows the simultaneous investigation of multiple metabolic pathways in a single HP ^{13}C-MRI. For instance, the copolarization of [1-^{13}C]pyruvate and [^{13}C,[15]N$_2$]urea provides comprehensive data on both pyruvate metabolism and tumor perfusion [62,63]. Overall, as research progresses, the clinical utilization of HP ^{13}C-MRI is expanding, as exemplified by the current exploration of HP ^{13}C-MRI for evaluating the immune potential in the spleen [56] or neck lymph nodes (Fig. 5B).

CONCLUSIONS

In summary, HP ^{13}C-MRI is an emerging technique with significant potential in the field of radiology. With its ability to monitor real-time metabolic changes, this imaging method can revolutionize disease diagnosis and treatment. Although still in its early developmental phases, initial studies have indicated its capacity to differentiate between benign and malignant tumors, monitor treatment responses, and potentially forecast patient outcomes. The ongoing evolution and increasing accessibility of this technology suggest a growing role for HP ^{13}C-MRI in the diagnosis, treatment, and care of patients with cancer. However, further research is required to optimize its functionality and validate its clinical usefulness. Despite the need for refinement, the prospective advantages are evident, indicating a promising future for this technology.

Supplement

The Supplement is available with this article at https://doi.org/10.3348/kjr.2024.0069.

Availability of Data and Material

Data sharing not applicable to this article as no datasets were generated or analyzed during the study.

Conflicts of Interest

The authors have no potential conflicts of interest to disclose.

Author Contributions

Conceptualization: Ying-Chieh Lai, Ching-Yi Hsieh, Kuan-Ying Lu, Gigin Lin. Data curation: all authors. Formal analysis: Ying-Chieh Lai, Ching-Yi Hsieh, Kuan-Ying Lu, Gigin Lin. Funding acquisition: Ying-Chieh Lai, Ching-Yi Hsieh, Yu-Hsiang Juan, Shu-Hang Ng, Yung-Liang Wan, Gigin Lin. Investigation: Ying-Chieh Lai, Ching-Yi Hsieh, Gigin Lin. Methodology: Ying-Chieh Lai, Ching-Yi Hsieh, Gigin Lin. Project administration: Kuan-Ying Lu, Hsien-Ju Lee. Resources: Gigin Lin. Software: Ying-Chieh Lai, Ching-Yi Hsieh. Supervision: Gigin Lin. Validation: Ying-Chieh Lai, Ching-Yi Hsieh. Visualization: Ying-Chieh Lai, Ching-Yi Hsieh. Writing—original draft: Ying-Chieh Lai, Gigin Lin. Writing—review & editing: all authors.

Table 4. ^{13}C-labeled probes and their potential applications

Probes	Potential clinical applications
[1-^{13}C]pyruvate*	Glycolysis
[2-^{13}C]pyruvate* [59-61]	Glycolysis, TCA cycle
[^{13}C,[15]N$_2$]urea* [62,63]	Perfusion
[1-^{13}C]α-ketoglutarate* [64]	TCA cycle, IDH
[1-^{13}C]1,2-glycerol carbonate* [65]	pH imaging
[^{13}C]bicarbonate [66]	pH imaging
[2-^{13}C]dihydroxyacetone [67]	Hepatic glycolysis, gluconeogenesis, and glycerol synthesis
[1,4-[13]C$_2$]fumarate [68]	Necrosis

*Indicate probes that have been clinically validated for human use.
TCA = tricarboxylic acid cycle, IDH = isocitrate dehydrogenase

ORCID IDs

Ying-Chieh Lai
https://orcid.org/0000-0003-0148-9488

Ching-Yi Hsieh
https://orcid.org/0000-0002-9475-5169

Yu-Hsiang Juan
https://orcid.org/0000-0002-1046-5309

Kuan-Ying Lu
https://orcid.org/0000-0002-4677-9000

Hsien-Ju Lee
https://orcid.org/0009-0009-0011-6592

Shu-Hang Ng
https://orcid.org/0000-0002-1842-6179

Yung-Liang Wan
https://orcid.org/0000-0002-3039-996X

Gigin Lin
https://orcid.org/0000-0001-7246-1058

REFERENCES

1. Ardenkjaer-Larsen JH, Fridlund B, Gram A, Hansson G, Hansson L, Lerche MH, et al. Increase in signal-to-noise ratio of > 10,000 times in liquid-state NMR. *Proc Natl Acad Sci U S A* 2003;100:10158-10163

2. Merritt ME, Harrison C, Storey C, Jeffrey FM, Sherry AD, Malloy CR. Hyperpolarized ^{13}C allows a direct measure of flux through a single enzyme-catalyzed step by NMR. *Proc Natl Acad Sci U S A* 2007;104:19773-19777

3. Gallagher FA, Bohndiek SE, Kettunen MI, Lewis DY, Soloviev D, Brindle KM. Hyperpolarized ^{13}C MRI and PET: in vivo tumor biochemistry. *J Nucl Med* 2011;52:1333-1336

4. Pantel AR, Ackerman D, Lee SC, Mankoff DA, Gade TP. Imaging cancer metabolism: underlying biology and emerging strategies. *J Nucl Med* 2018;59:1340-1349

5. Mosessian S, Duarte-Vogel SM, Stout DB, Roos KP, Lawson GW, Jordan MC, et al. INDs for PET molecular imaging probes-approach by an academic institution. *Mol Imaging Biol* 2014;16:441-448

6. Ardenkjaer-Larsen JH, Leach AM, Clarke N, Urbahn J, Anderson D, Skloss TW. Dynamic nuclear polarization polarizer for sterile use intent. *NMR Biomed* 2011;24:927-932

7. Hu KN. Polarizing agents and mechanisms for high-field dynamic nuclear polarization of frozen dielectric solids. *Solid State Nucl Magn Reson* 2011;40:31-41

8. Hovav Y, Feintuch A, Vega S. Theoretical aspects of dynamic nuclear polarization in the solid state–spin temperature and thermal mixing. *Phys Chem Chem Phys* 2013;15:188-203

9. National Cancer Institute. Hyperpolarized pyruvate ^{13}C injection investigator's brochure [accessed on February 14, 2024]. Available at: https://imaging.cancer.gov/programs_resources/cancer-tracer-synthesis-resources/docs/c13_pyruvate_IB_PDF.pdf

10. Deh K, Zhang G, Park AH, Cunningham CH, Bragagnolo ND, Lyashchenko S, et al. First in-human evaluation of [1-^{13}C] pyruvate in D_2O for hyperpolarized MRI of the brain: a safety and feasibility study. *Magn Reson Med* 2024;91:2559-2567

11. Sacolick LI, Sun L, Vogel MW, Dixon WT, Hancu I. Fast radiofrequency flip angle calibration by Bloch-Siegert shift. *Magn Reson Med* 2011;66:1333-1338

12. Schulte RF, Sacolick L, Deppe MH, Janich MA, Schwaiger M, Wild JM, et al. Transmit gain calibration for nonproton MR using the Bloch-Siegert shift. *NMR Biomed* 2011;24:1068-1072

13. Larson PEZ, Gordon JW. Hyperpolarized metabolic MRI—acquisition, reconstruction, and analysis methods. *Metabolites* 2021;11:386

14. Yen YF, Kohler SJ, Chen AP, Tropp J, Bok R, Wolber J, et al. Imaging considerations for in vivo ^{13}C metabolic mapping using hyperpolarized ^{13}C-pyruvate. *Magn Reson Med* 2009;62:1-10

15. Mayer D, Levin YS, Hurd RE, Glover GH, Spielman DM. Fast metabolic imaging of systems with sparse spectra: application for hyperpolarized ^{13}C imaging. *Magn Reson Med* 2006;56:932-937

16. Ramirez MS, Lee J, Walker CM, Sandulache VC, Hennel F, Lai SY, et al. Radial spectroscopic MRI of hyperpolarized [1-^{13}C] pyruvate at 7 tesla. *Magn Reson Med* 2014;72:986-995

17. Jiang W, Lustig M, Larson PE. Concentric rings K-space trajectory for hyperpolarized ^{13}C MR spectroscopic imaging. *Magn Reson Med* 2016;75:19-31

18. Wiesinger F, Weidl E, Menzel MI, Janich MA, Khegai O, Glaser SJ, et al. IDEAL spiral CSI for dynamic metabolic MR imaging of hyperpolarized [1-^{13}C]pyruvate. *Magn Reson Med* 2012;68:8-16

19. Meyer CH, Pauly JM, Macovski A, Nishimura DG. Simultaneous spatial and spectral selective excitation. *Magn Reson Med* 1990;15:287-304

20. Lau AZ, Chen AP, Hurd RE, Cunningham CH. Spectral-spatial excitation for rapid imaging of DNP compounds. *NMR Biomed*

2011;24:988-996

21. Xing Y, Reed GD, Pauly JM, Kerr AB, Larson PE. Optimal variable flip angle schemes for dynamic acquisition of exchanging hyperpolarized substrates. *J Magn Reson* 2013;234:75-81

22. Bankson JA, Walker CM, Ramirez MS, Stefan W, Fuentes D, Merritt ME, et al. Kinetic modeling and constrained reconstruction of hyperpolarized [1-^{13}C]-pyruvate offers improved metabolic imaging of tumors. *Cancer Res* 2015;75:4708-4717

23. Harrison C, Yang C, Jindal A, DeBerardinis RJ, Hooshyar MA, Merritt M, et al. Comparison of kinetic models for analysis of pyruvate-to-lactate exchange by hyperpolarized ^{13}C NMR. *NMR Biomed* 2012;25:1286-1294

24. Hill DK, Orton MR, Mariotti E, Boult JK, Panek R, Jafar M, et al. Model free approach to kinetic analysis of real-time hyperpolarized ^{13}C magnetic resonance spectroscopy data. *PLoS One* 2013;8:e71996

25. Miloushev VZ, Granlund KL, Boltyanskiy R, Lyashchenko SK, DeAngelis LM, Mellinghoff IK, et al. Metabolic imaging of the human brain with hyperpolarized ^{13}C pyruvate demonstrates ^{13}C lactate production in brain tumor patients. *Cancer Res* 2018;78:3755-3760

26. Autry AW, Gordon JW, Chen HY, LaFontaine M, Bok R, Van Criekinge M, et al. Characterization of serial hyperpolarized ^{13}C metabolic imaging in patients with glioma. *Neuroimage Clin* 2020;27:102323

27. Autry AW, Park I, Kline C, Chen HY, Gordon JW, Raber S, et al. Pilot study of hyperpolarized ^{13}C metabolic imaging in pediatric patients with diffuse intrinsic pontine glioma and other CNS cancers. *AJNR Am J Neuroradiol* 2021;42:178-184

28. Lee CY, Soliman H, Bragagnolo ND, Sahgal A, Geraghty BJ, Chen AP, et al. Predicting response to radiotherapy of intracranial metastases with hyperpolarized ^{13}C MRI. *J Neurooncol* 2021;152:551-557

29. Chen J, Patel TR, Pinho MC, Choi C, Harrison CE, Baxter JD, et al. Preoperative imaging of glioblastoma patients using hyperpolarized ^{13}C pyruvate: potential role in clinical decision making. *Neurooncol Adv* 2021;3:vdab092

30. Zaccagna F, McLean MA, Grist JT, Kaggie J, Mair R, Riemer F, et al. Imaging glioblastoma metabolism by using hyperpolarized [1-^{13}C]pyruvate demonstrates heterogeneity in lactate labeling: a proof of principle study. *Radiol Imaging Cancer* 2022;4:e210076

31. Grist JT, McLean MA, Riemer F, Schulte RF, Deen SS, Zaccagna F, et al. Quantifying normal human brain metabolism using hyperpolarized [1-^{13}C]pyruvate and magnetic resonance imaging. *Neuroimage* 2019;189:171-179

32. Lee CY, Soliman H, Geraghty BJ, Chen AP, Connelly KA, Endre R, et al. Lactate topography of the human brain using hyperpolarized ^{13}C-MRI. *Neuroimage* 2020;204:116202

33. Hackett EP, Pinho MC, Harrison CE, Reed GD, Liticker J, Raza J, et al. Imaging acute metabolic changes in patients with mild traumatic brain injury using hyperpolarized [1-^{13}C]pyruvate. *iScience* 2020;23:101885

34. Ma J, Pinho MC, Harrison CE, Chen J, Sun C, Hackett EP, et al. Dynamic ^{13}C MR spectroscopy as an alternative to imaging for assessing cerebral metabolism using hyperpolarized pyruvate in humans. *Magn Reson Med* 2022;87:1136-1149

35. Uthayakumar B, Soliman H, Bragagnolo ND, Cappelletto NIC, Lee CY, Geraghty B, et al. Age-associated change in pyruvate metabolism investigated with hyperpolarized ^{13}C-MRI of the human brain. *Hum Brain Mapp* 2023;44:4052-4063

36. Cunningham CH, Lau JY, Chen AP, Geraghty BJ, Perks WJ, Roifman I, et al. Hyperpolarized ^{13}C metabolic MRI of the human heart: initial experience. *Circ Res* 2016;119:1177-1182

37. Rider OJ, Apps A, Miller JJJJ, Lau JYC, Lewis AJM, Peterzan MA, et al. Noninvasive in vivo assessment of cardiac metabolism in the healthy and diabetic human heart using hyperpolarized ^{13}C MRI. *Circ Res* 2020;126:725-736

38. Park JM, Reed GD, Liticker J, Putnam WC, Chandra A, Yaros K, et al. Effect of doxorubicin on myocardial bicarbonate production from pyruvate dehydrogenase in women with breast cancer. *Circ Res* 2020;127:1568-1570

39. Ma J, Malloy CR, Pena S, Harrison CE, Ratnakar J, Zaha VG, et al. Dual-phase imaging of cardiac metabolism using hyperpolarized pyruvate. *Magn Reson Med* 2022;87:302-311

40. Park JM, Harrison CE, Ma J, Chen J, Ratnakar J, Zun Z, et al. Hyperpolarized ^{13}C MR spectroscopy depicts in vivo effect of exercise on pyruvate metabolism in human skeletal muscle. *Radiology* 2021;300:626-632

41. Woitek R, McLean MA, Gill AB, Grist JT, Provenzano E, Patterson AJ, et al. Hyperpolarized ^{13}C MRI of tumor metabolism demonstrates early metabolic response to neoadjuvant chemotherapy in breast cancer. *Radiol Imaging Cancer* 2020;2:e200017

42. Woitek R, McLean MA, Ursprung S, Rueda OM, Manzano Garcia R, Locke MJ, et al. Hyperpolarized carbon-13 MRI for early response assessment of neoadjuvant chemotherapy in breast cancer patients. *Cancer Res* 2021;81:6004-6017

43. Tran M, Latifoltojar A, Neves JB, Papoutsaki MV, Gong F, Comment A, et al. First-in-human in vivo non-invasive assessment of intra-tumoral metabolic heterogeneity in renal cell carcinoma. *BJR Case Rep* 2019;5:20190003

44. Tang S, Meng MV, Slater JB, Gordon JW, Vigneron DB, Stohr BA, et al. Metabolic imaging with hyperpolarized ^{13}C pyruvate magnetic resonance imaging in patients with renal tumors-initial experience. *Cancer* 2021;127:2693-2704

45. Ursprung S, Woitek R, McLean MA, Priest AN, Crispin-Ortuzar M, Brodie CR, et al. Hyperpolarized ^{13}C-pyruvate metabolism as a surrogate for tumor grade and poor outcome in renal cell carcinoma—a proof of principle study. *Cancers (Basel)* 2022;14:335

46. Lee PM, Chen HY, Gordon JW, Wang ZJ, Bok R, Hashoian R, et al. Whole-abdomen metabolic imaging of healthy volunteers using hyperpolarized [1-^{13}C]pyruvate MRI. *J Magn Reson imaging* 2022;56:1792-1806

47. Stødkilde-Jørgensen H, Laustsen C, Hansen ESS, Schulte R, Ardenkjaer-Larsen JH, Comment A, et al. Pilot study experiences

with hyperpolarized [1-^{13}C]pyruvate MRI in pancreatic cancer patients. *J Magn Reson Imaging* 2020;51:961-963

48. Gordon JW, Chen HY, Nickles T, Lee PM, Bok R, Ohliger MA, et al. Hyperpolarized ^{13}C metabolic MRI of patients with pancreatic ductal adenocarcinoma. *J Magn Reson Imaging* 2023 Dec 2 [Epub]. https://doi.org/10.1002/jmri.29162

49. Nelson SJ, Kurhanewicz J, Vigneron DB, Larson PE, Harzstark AL, Ferrone M, et al. Metabolic imaging of patients with prostate cancer using hyperpolarized [1-^{13}C]pyruvate. *Sci Transl Med* 2013;5:198ra108

50. Aggarwal R, Vigneron DB, Kurhanewicz J. Hyperpolarized 1-[^{13}C]-pyruvate magnetic resonance imaging detects an early metabolic response to androgen ablation therapy in prostate cancer. *Eur Urol* 2017;72:1028-1029

51. Chen HY, Aggarwal R, Bok RA, Ohliger MA, Zhu Z, Lee P, et al. Hyperpolarized ^{13}C-pyruvate MRI detects real-time metabolic flux in prostate cancer metastases to bone and liver: a clinical feasibility study. *Prostate Cancer Prostatic Dis* 2020;23:269-276

52. Granlund KL, Tee SS, Vargas HA, Lyashchenko SK, Reznik E, Fine S, et al. Hyperpolarized MRI of human prostate cancer reveals increased lactate with tumor grade driven by monocarboxylate transporter 1. *Cell Metab* 2020;31:105-114.e3

53. de Kouchkovsky I, Chen HY, Ohliger MA, Wang ZJ, Bok RA, Gordon JW, et al. Hyperpolarized 1-[^{13}C]-pyruvate magnetic resonance imaging detects an early metabolic response to immune checkpoint inhibitor therapy in prostate cancer. *Eur Urol* 2022;81:219-221

54. Chen HY, Bok RA, Cooperberg MR, Nguyen HG, Shinohara K, Westphalen AC, et al. Improving multiparametric MR-transrectal ultrasound guided fusion prostate biopsies with hyperpolarized ^{13}C pyruvate metabolic imaging: a technical development study. *Magn Reson Med* 2022;88:2609-2620

55. Sushentsev N, McLean MA, Warren AY, Benjamin AJV, Brodie C, Frary A, et al. Hyperpolarised ^{13}C-MRI identifies the emergence of a glycolytic cell population within intermediate-risk human prostate cancer. *Nat Commun* 2022;13:466

56. Lin G, Hsieh CY, Lai YC, Wang CC, Lin Y, Lu KY, et al. Hyperpolarized [1-^{13}C]-pyruvate MRS evaluates immune potential and predicts response to radiotherapy in cervical cancer. *Eur Radiol Exp* 2024;8:46

57. Gallagher FA, Woitek R, McLean MA, Gill AB, Manzano Garcia R, Provenzano E, et al. Imaging breast cancer using hyperpolarized carbon-13 MRI. *Proc Natl Acad Sci U S A* 2020;117:2092-2098

58. Ye Z, Song B, Lee PM, Ohliger MA, Laustsen C. Hyperpolarized carbon 13 MRI in liver diseases: recent advances and future opportunities. *Liver Int* 2022;42:973-983

59. Hu S, Yoshihara HA, Bok R, Zhou J, Zhu M, Kurhanewicz J, et al. Use of hyperpolarized [1-^{13}C]pyruvate and [2-^{13}C]pyruvate to probe the effects of the anticancer agent dichloroacetate on mitochondrial metabolism in vivo in the normal rat. *Magn Reson Imaging* 2012;30:1367-1372

60. Schroeder MA, Atherton HJ, Ball DR, Cole MA, Heather LC, Griffin JL, et al. Real-time assessment of Krebs cycle metabolism using hyperpolarized ^{13}C magnetic resonance spectroscopy. *FASEB J* 2009;23:2529-2538

61. Chung BT, Chen HY, Gordon J, Mammoli D, Sriram R, Autry AW, et al. First hyperpolarized [2-^{13}C]pyruvate MR studies of human brain metabolism. *J Magn Reson* 2019;309:106617

62. Qin H, Tang S, Riselli AM, Bok RA, Delos Santos R, van Criekinge M, et al. Clinical translation of hyperpolarized ^{13}C pyruvate and urea MRI for simultaneous metabolic and perfusion imaging. *Magn Reson Med* 2022;87:138-149

63. Liu X, Tang S, Mu C, Qin H, Cui D, Lai YC, et al. Development of specialized magnetic resonance acquisition techniques for human hyperpolarized [^{13}C,^{15}N$_2$]urea + [1-^{13}C]pyruvate simultaneous perfusion and metabolic imaging. *Magn Reson Med* 2022;88:1039-1054

64. Chaumeil MM, Larson PE, Yoshihara HA, Danforth OM, Vigneron DB, Nelson SJ, et al. Non-invasive in vivo assessment of IDH1 mutational status in glioma. *Nat Commun* 2013;4:2429

65. Korenchan DE, Flavell RR, Baligand C, Sriram R, Neumann K, Sukumar S, et al. Dynamic nuclear polarization of biocompatible ^{13}C-enriched carbonates for in vivo pH imaging. *Chem Commun (Camb)* 2016;52:3030-3033

66. Gallagher FA, Kettunen MI, Day SE, Hu DE, Ardenkjaer-Larsen JH, Zandt Ri, et al. Magnetic resonance imaging of pH in vivo using hyperpolarized ^{13}C-labelled bicarbonate. *Nature* 2008;453:940-943

67. Marco-Rius I, Wright AJ, Hu DE, Savic D, Miller JJ, Timm KN, et al. Probing hepatic metabolism of [2-^{13}C]dihydroxyacetone in vivo with ^{1}H-decoupled hyperpolarized ^{13}C-MR. *MAGMA* 2021;34:49-56

68. Gallagher FA, Kettunen MI, Hu DE, Jensen PR, Zandt RI, Karlsson M, et al. Production of hyperpolarized [1,4-^{13}C$_2$]malate from [1,4-^{13}C$_2$]fumarate is a marker of cell necrosis and treatment response in tumors. *Proc Natl Acad Sci U S A* 2009;106:19801-19806

Supplementary Table 1. Summary of quantitative results from human studies using HP ^{13}C-MRI

Authors*	Clinical applications	Quantitative results	Additional results
Brain			
Miloushev et al., 2018 [25]	1st human brain tumor study	*Kinetic modeling* Whole brain: k_{PL} = 0.12	Higher production of Pyr and Lac in normal cortical/subcortical regions; glycolytic heterogeneity among different brain tumors
Autry et al., 2020 [26]	Post radio-chemotherapy follow-up in infiltrative glioma	*Kinetic modeling* Glioma patient Normal brain: k_{PL} = 0.020, k_{PB} = 0.006; normal brain post bevacizumab: k_{PL} = 0.047, k_{PB} = 0.011; glioma (contrast enhancing): k_{PL} = 0.032–0.041; glioma (T2 hyperintense): k_{PL} = 0.024 Healthy volunteer Normal brain: k_{PL} = 0.018, k_{PB} = 0.004	Global elevation of k_{PL} and k_{PB} post bevacizumab; elevated k_{PL} and k_{PB} in progressive disease
Autry et al., 2021 [27]	Pediatric brain tumor vs. normal brain, pediatric safety profile	*Model free* Whole brain: SNR$_{Pyr}$ = 7.85 x 10^2–3.52 x 10^5, SNR$_{Lac}$ = 1.75 x 10^2–7.20 x 10^4, SNR$_{Bic}$ = 64–1.52 x 10^4	Safety of HP ^{13}C-MRI in pediatric patients
Lee et al., 2021 [28]	Prediction of radiotherapy response in intracranial metastases	*Model free* z-score = -2.33–3.74	Tumors with highest z-scores are associated with radiotherapy failure
Chen et al., 2021 [29]	Glioblastoma vs. normal brain	*Model free* Glioblastoma: Lac/TC = 0.310, Bic/TC = 0.086; normal brain: Lac/TC = 0.246, Bic/TC = 0.108	1st vs. 2nd injections: metabolites/TC were insignificantly higher in 2nd injection
Zaccagna et al., 2022 [30]	Glioblastoma vs. normal brain	*Kinetic modeling* (x10^{-3}) Glioblastoma: k_{PL} = 16.1, k_{PB} = 1.7; normal brain: k_{PL} = 16.5, k_{PB} = 2.4 *Model free* Glioblastoma: Lac/Pyr = 0.34, Bic/Pyr = 0.06; normal brain: Lac/Pyr = 0.36, Bic/Pyr = 0.10	Bic/Pyr negatively correlates with lesion volume and volume of enhancing tissue; Bic/Pyr positively correlates with percentage of non-enhancing core; LDHA positively correlates with Lac/Pyr; MCT4 positively correlates with Bic/Pyr and Bic/Lac
Grist et al., 2019 [31]	Technical feasibility in healthy human brain	*Kinetic modeling* Whole brain: k_{PL} = 0.012, k_{PB} = 0.002	Higher metabolites signal in gray matter compared to white matter
Lee et al., 2020 [32]	Metabolite topography in healthy human brain	Not available	Lac topography unveils a region-specific distribution of Lac in the brain, which is consistent across individuals
Hackett et al., 2020 [33]	Traumatic brain injury	*Model free* Patient 1: trauma vs normal: Bic/TC = 0.027 vs. 0.059, Lac/TC = 0.236 vs. 0.191 Patient 2: trauma vs normal: Bic/TC = 0.025 vs. 0.047, Lac/TC = 0.164 vs. 0.162	Mild traumatic brain injury without discernible anatomic change or hemorrhage on MRI
Ma et al., 2022 [34]	Technical feasibility in healthy human brain	*Kinetic modeling* Whole brain: k_{PL} = 0.014–0.018, k_{PB} = 0.004–0.006 *Model free* Whole brain: Lac/TC = 0.21–0.24, Bic/TC = 0.065–0.091	Lac/TC and Bic/TC linearly correlate with fractional gray matter volume
Uthayakumar et al., 2023 [35]	Metabolic changes in brain aging	*Model free* A 7% ± 2% decrease per decade for Lac and a 9% ± 4% decrease per decade for Bic	Variability in aging-related metabolic changes is observed across different brain regions
Heart and skeletal muscle			
Cunningham et al., 2016 [36]	1st human healthy heart study	*Model free* SNR$_{Pyr}$ = 115, SNR$_{Bic}$ = 56, SNR$_{Lac}$ = 53	Pyr signal observed only in cardiac chamber, Bic only in myocardium, Lac in both chamber and myocardium
Rider et al., 2020 [37]	Healthy vs. diabetic heart	*Model free* (x 10^{-2}) Healthy heart: Bic/Pyr = 0.84, Lac/Pyr = 5.16, Ala/Pyr = 3.17; diabetic heart: Bic/Pyr = 0.16, Lac/Pyr = 8.51, Ala/Pyr = 3.82	Significantly increased Pyr-to-Bic flux after oral glucose challenge
Park et al., 2020 [38]	Cardiotoxicity of doxorubicin	*Model free* Before doxorubicin: Bic/TC = 0.036, Lac/TC = 0.448, Ala/TC = 0.045; after doxorubicin: Bic/TC = 0.032, Lac/TC = 0.440, Ala/TC = 0.045	Hemoglobin, high-sensitivity troponin, and left ventricular global longitudinal strain also change after chemotherapy
Ma et al., 2022 [39]	End diastolic vs. end systolic in healthy heart	*Model free* End diastolic to end systolic: Bic/Lac = 21.6 decrease, Bic/Ala = 9.4 decrease	The decrease in Bic/Lac from end diastolic to end systolic occurs prominently in the mid-anterior and mid-inferoseptal segments of heart
Park et al., 2021 [40]	Rest vs. exercise vs. recovery in healthy calf skeletal muscle	*Model free* Rest: Lac/TC = 0.18, Bic/TC = 0.004; exercise: Lac/TC = 0.31, Bic/TC = 0.036; recovery: Lac/TC = 0.42, Bic/TC = 0.002	TC (perfusion) at rest increases to 2.8-fold with exercise and to 3.2-fold during recovery
Body and oncology			
Woitek et al., 2020 [41]	Post neoadjuvant chemotherapy follow-up in breast cancer	*Kinetic modeling* 37% decrease in k_{PL} after neoadjuvant chemotherapy *Model free* 34% decrease in Lac/Pyr after neoadjuvant chemotherapy	After neoadjuvant chemotherapy 76% decrease in tumor volume but 132% increase in K^{trans} and 31% increase in k_{ep}; pathologic complete response after neoadjuvant chemotherapy
Woitek et al., 2021 [42]	Very early neoadjuvant chemotherapy response assessment in breast cancer	*Kinetic modeling* Breast cancer post chemotherapy k_{PL} = 0.0064 → 0.0079 *Model free* Breast cancer post chemotherapy: SNR$_{Pyr}$ = 19.7 → 16.5, SNR$_{Lac}$ = 7.0 → 4.5, Lac/Pyr = 0.28 → 0.34	≥ 20% increase of Lac/Pyr predicts pathologic complete response
Tran et al., 2019 [43]	Intratumoral metabolic heterogeneity of RCC	Not available	Variability in Lac signal correlates with Lac levels in tumor samples on LC-MS analysis
Tang et al., 2021 [44]	Tumor grade and histopathologic type of RCC	*Model free* Lac/Pyr: chromophobe RCC > grade 3 ccRCC > grade 2 ccRCC	Demonstration of good reproducibility of HP ^{13}C-MRI by performing 2 acquisitions in the same day
Ursprung et al., 2022 [45]	Prediction of tumor grade of RCC	*Kinetic modeling* (median) k_{PL}: ccRCC = 0.0065, normal kidney = 0.0043, liposarcoma = 0.0152, pheochromocytoma = 0.0086, oncocytoma = 0.0022 *Model free* (median) SNR$_{Pyr}$: ccRCC = 26.7, normal kidney = 30.1, liposarcoma = 31.9, pheochromocytoma = 34.0, oncocytoma = 12.3; SNR$_{Lac}$: ccRCC = 5.7, normal kidney = 3.4, liposarcoma = 10.5, pheochromocytoma = 6.0, oncocytoma = 1.0; Lac/Pyr: ccRCC = 0.13, normal kidney = 0.14, liposarcoma = 0.35, pheochromocytoma = 0.17, oncocytoma = 0.14	Increasing k_{PL} correlates with higher tumor grade; Lac/Pyr negatively correlates with ADC; MCT1 expression (but not MCT4) positively correlates with k_{PL}; MCT1 expression independently predicts overall survival of RCC patients
Lee et al., 2022 [46]	Comparison among normal intrabdominal solid organs: liver, kidney, pancreas, spleen	*Kinetic modeling* k_{PL}: liver = 0.019, kidney (R) = 0.0036, kidney (L) = 0.0033, pancreas = 0.0063, spleen = 0.0096; k_{PA}: liver = 0.012, kidney (R) = 0.0011, kidney (L) = 0.00087, pancreas = 0.0034, spleen = 0.00073	The liver exhibits a comparatively lower absolute metabolite signal, yet the highest metabolite conversion rates
Stødkilde-Jørgensen et al., 2020 [47]	Tumor vs. normal in pancreatic cancer	*Model free* Pancreatic cancer: Ala/Lac = 0.33; normal pancreas: Ala/Lac = 0.23	Ala/Lac as a potential biomarker to detect pancreatic ancer
Gordon et al., 2023 [48]	Tumor vs. normal, early response prediction in pancreatic cancer	*Model free* Pancreatic cancer: Lac/Pyr = 0.30–1.65, Ala/Pyr = < 0.01–0.14, Ala/Lac = < 0.01–0.46; normal pancreas: Lac/Pyr = 0.20–0.27, Ala/Pyr = 0.06–0.15, Ala/Lac = 0.24–0.79	Early metabolic response at 4 weeks correlates with subsequent tumor response
Nelson et al., 2013 [49]	Tumor vs. normal in prostate cancer	*Kinetic modeling* Prostate cancer: k_{PL} = 0.013	1st human study in prostate cancer, safety profile
Aggarwal et al., 2017 [50]	Early response for androgen deprivation therapy in prostate cancer	*Kinetic modeling* Prostate cancer post androgen deprivation therapy: k_{PL} = 0.025 → 0.007	Only modest changes in tumor size and ADC value
Chen et al., 2020 [51]	Feasibility in bone and liver metastasis in castration-resistant prostate cancer	*Kinetic modeling* Bone metastases: k_{PL} = 0.020; liver metastases: k_{PL} = 0.026; liver metastasis post chemotherapy: k_{PL} = 0.026 → 0.015 *Model free* Bone metastasis: SNR$_{TC}$ = 117; liver metastasis: SNR$_{TC}$ = 85	RNA-seq found higher LDHA expression relative to the dominant isoform of LDH
Granlund et al., 2020 [52]	Tumor grade of prostate cancer	*Model free* max Lac/TC = 0.35 Time to max Lac/TC = 44 s	Lac increases with Gleason tumor grade; regions exhibiting high Lac also show high MCT1 expression and loss of PTEN
de Kouchkovsky et al., 2022 [53]	Early immunotherapy response assessment in castration-resistant prostate cancer	*Kinetic modeling* Prostate cancer post immunotherapy: k_{PL} = 0.0273 → undetectable, k_{PL} = 0.0147 → 0.0006	Metabolic response is more significant than morphologic response
Chen et al., 2022 [54]	Integration with MR/TRUS fusion-guided biopsy in prostate cancer	*Kinetic modeling* k_{PL} > 0.02 as biomarker of suspected cancer; prostate cancer: k_{PL} = 0.0319; normal prostate: k_{PL} = 0.0110	4 of 6 k_{PL} targets on HP ^{13}C-MRI did not correlate to PIRDAS targets on conventional MRI
Sushentsev et al., 2022 [55]	Metabolic phenotyping in intermediate risk prostate cancer	*Kinetic modeling* Prostate cancer: k_{PL} = 0.011 *Model free* Prostate cancer: SNR$_{Lac}$ = 12, SNR$_{Pyr}$ = 33, SNR$_{TC}$ = 53	SNR$_{Lac}$ positively correlates to % Gleason pattern 4 and mean ADC values
Lin et al., 2024 [56]	Immune activation of spleen post chemoradiotherapy	*Model free* (x 10^{-2}) Responder: Pyr/TC = 91.5, Lac/TC = 3.6; nonresponder: Pyr/TC = 74.4, Lac/TC = 19.9	Lower baseline metabolism in spleen correlates with better response to chemoradiotherapy

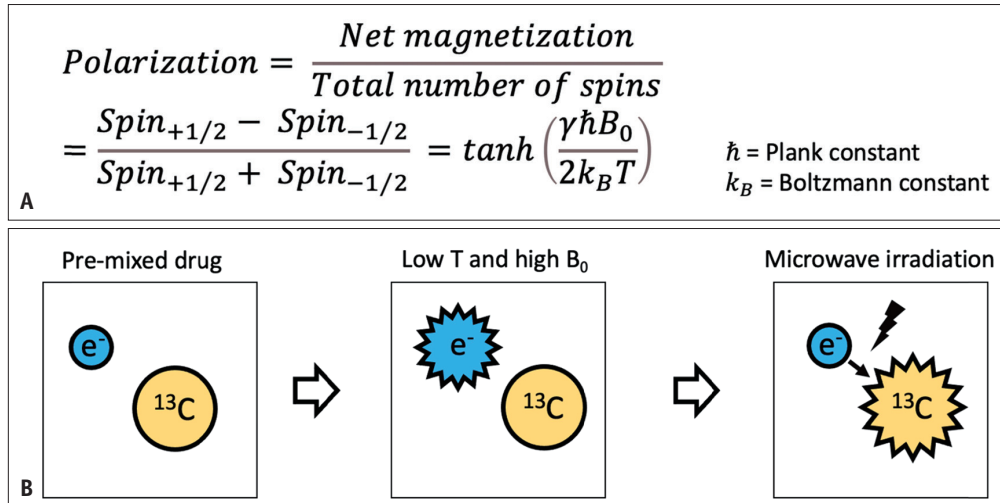Unless specified otherwise, data are presented as mean values.

*The numbers enclosed in brackets correspond to the numbers of the articles listed in the reference section of the main paper.

HP = hyperpolarized, Pyr = pyruvate, Lac = lactate, Ala = alanine, Bic = bicarbonate, TC = total carbon, SNR = signal-to-noise ratio, LDH = lactate dehydrogenase (isoform: LDHA), MCT = monocarboxylate transporter (isoform: MCT1, MCT4), RCC = renal cell carcinoma, cc = clear cell, ADC = apparent diffusion coefficient, TRUS = transrectal ultrasound
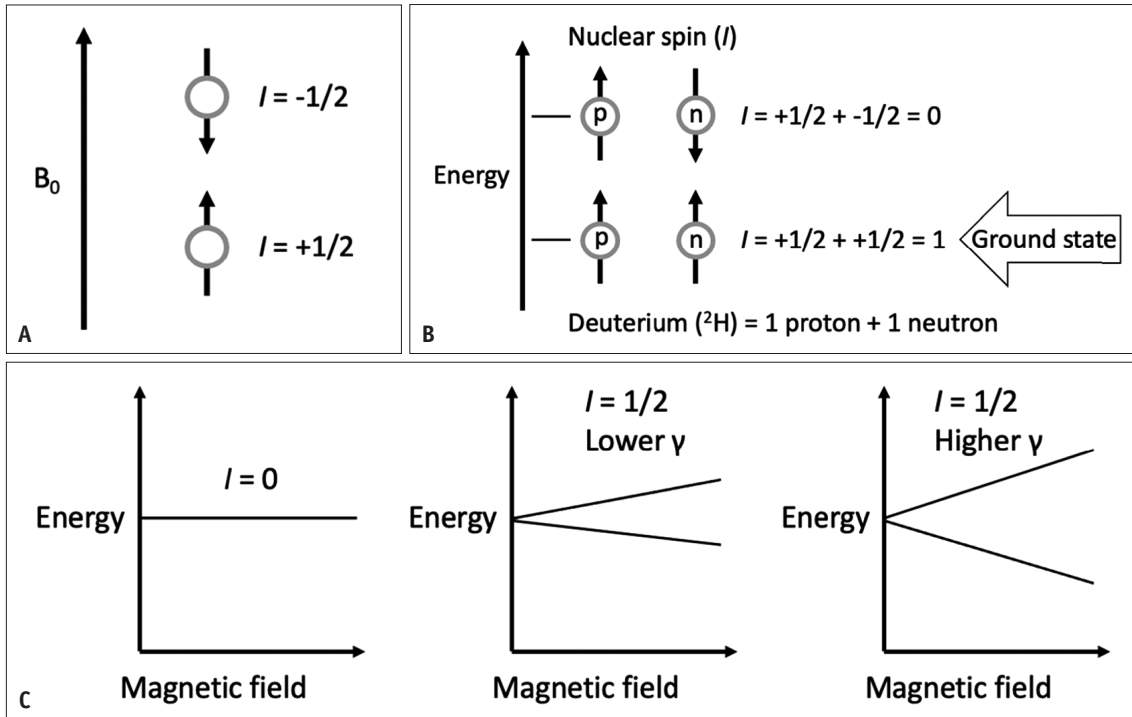
Supplementary Fig. 1. Fundamental principles of nuclear spin. **A:** Nuclear spin is an intrinsic property of particles, always manifesting as either +1/2 or -1/2. **B:** In nature, nuclear spin results from the combined spins of protons and neutrons, existing exclusively in the ground state (I) with values such as 0, 1/2, 1, 3/2, and so on. **C:** The ground state comprises "$2I + 1$" sublevels. Upon the application of a magnetic field, slight energy differences arise between these sublevels, leading to Zeeman splitting. Nuclei with $I = 0$ exhibit only one sublevel, lack Zeeman splitting, and remain inactive in MRI (^{12}C), whereas nuclei with $I \neq 0$ (^1H and ^{13}C) are nuclear magnetic resonance active due to having multiple sublevels. Notably, nuclei with higher gyromagnetic ratios (γ) experience more significant splitting when a magnetic field is applied.

$$Polarization = \frac{Net\ magnetization}{Total\ number\ of\ spins}$$

$$= \frac{Spin_{+1/2} - Spin_{-1/2}}{Spin_{+1/2} + Spin_{-1/2}} = tanh\left(\frac{\gamma \hbar B_0}{2k_B T}\right)$$

$\hbar$ = Plank constant
k_B = Boltzmann constant

A

B

| Pre-mixed drug | Low T and high B$_0$ | Microwave irradiation |

Supplementary Fig. 2. Basic concepts of DNP. **A:** Polarization is a function of gyromagnetic ration (γ), magnitude of magnetic field (B$_0$), and temperature (T). To polarize nuclei with lower γ, higher magnetic field and lower temperature environment are required. For example, clinical polarizer SPINlab^{TM} operates at B$_0$ = 5T and T = 0.8 k. **B:** Directly polarizing the ^{13}C nucleus (the brute force method) presents an engineering challenge and is time-consuming, making it impractical for clinical use. Electrons have a high γ of 28025 and are more amenable to polarization. DNP offers a clinically feasible solution by transferring polarization from electrons to ^{13}C nuclei, achieving 20%–30% ^{13}C polarization (equivalent to > 10000 signal enhancement) within 2–3 hours. DNP = dynamic nuclear polarization